

A Comprehensive Characterization of Empirical Parameterizations for OH Exposure in the Aerodyne Potential Aerosol Mass Oxidation Flow Reactor (PAM-OFR)

Qianying Liu^{1,2}, Dan Dan Huang^{2,*}, Andrew T. Lambe³, Shengrong Lou², Lulu Zeng¹, Yuhang Wu², Congyan Huang², Shikang Tao², Xi Cheng⁴, Qi Chen⁵, Ka In Hoi¹, Hongli Wang², Kai Meng Mok¹, Cheng Huang^{2,6}, Yong Jie Li^{1,*}

¹Department of Civil and Environmental Engineering, Department of Ocean Science and Technology, and Centre for Regional Oceans, Faculty of Science and Technology, University of Macau, Taipa, Macau SAR, 999078, China

²State Environmental Protection Key Laboratory of Formation and Prevention of Urban Air Pollution Complex, Shanghai Academy of Environmental Sciences, Shanghai, 200233, China

³Aerodyne Research Inc., Billerica, Massachusetts, 01821, United States

⁴School of Chemical and Environmental Engineering, China University of Mining and Technology (Beijing), Beijing 100083, China

⁵State Key Joint Laboratory of Environmental Simulation and Pollution Control, BIC-ESAT and IJRC, College of Environmental Sciences and Engineering, Peking University, Beijing, China

⁶State Ecology and Environment Scientific Observation and Research Station for the Yangtze River Delta at Dianshan Lake, Shanghai Environmental Monitoring Center, Shanghai, 200030, China

Correspondence to: Dan Dan Huang (huangdd@saes.sh.cn), Yong Jie Li (yongjieli@um.edu.mo)

Abstract. The oxidation flow reactor (OFR) has been widely used to simulate secondary organic aerosol (SOA) formation in laboratory and field studies. OH exposure (OH_{exp}), representing the extent of hydroxyl radical (OH) oxidation and normally expressed as the product of OH concentration and residence time in the OFR, is important in assessing the oxidation chemistry in SOA formation. Several models have been developed to quantify the OH_{exp} in OFRs, and empirical equations have been proposed to parameterize OH_{exp} . Practically, the empirical equations and the associated parameters are derived under atmospheric relevant conditions (i.e., external OH reactivity) with limited variations of calibration conditions, such as residence time, water vapor mixing ratio, O_3 concentration, etc. Whether the equations or parameters derived under limited sets of calibration conditions can accurately predict the OH_{exp} under dynamically changing experimental conditions with large variations (i.e., extremely high external OH reactivity) in real applications remains uncertain. In this study, we conducted 62 sets of experiments (416 data points) under a wide range of experimental conditions to evaluate the scope of the application of the empirical equations to estimate OH_{exp} . Sensitivity tests were also conducted to obtain a minimum number of data points that is necessary for generating the fitting parameters. We showed that, for the OFR185 mode (185-nm lamps with internal O_3 generation), except for external OH reactivity, the parameters obtained within a narrow range of calibration conditions can be extended to estimate the OH_{exp} when the experiments are in wider ranges of conditions. For example, parameters derived within a narrow water vapor mixing ratio range (0.49–0.99 %, corresponding to 15.1–30.8 % of relative humidity at 101.325 kPa and 298 K) can be extended to estimate the OH_{exp} under the entire range of water vapor mixing ratios (0.49–2.76 %,

equivalent to 15.1–85.7 % of relative humidity under identical conditions). However, the parameters obtained when the external OH reactivity is below 23 s^{-1} could not be used to reproduce the OH_{exp} under the entire range of external OH reactivity (4–204 s^{-1}). For the OFR254 mode (254-nm lamps with external O_3 generation), all parameters obtained within a narrow range of conditions can be used to estimate OH_{exp} accurately when experimental conditions are extended. Additionally, when using the OFR254 mode, too-low lamp voltages should be avoided, as they will generally result in large deviations in the estimations of OH_{exp} from empirical equations. Regardless of OFR185 or OFR254 mode, at least 20–30 data points from sulfur dioxide (SO_2) or (carbon monoxide) CO decay with varying conditions are required to fit a set of empirical parameters that can accurately estimate OH_{exp} . Caution should be exercised to use fitted parameters from low external OH reactivity to high ones, for instance, those from direct emissions such as vehicular exhaust and biomass burning.

1 Introduction

As the most important oxidant in tropospheric chemistry (Ehhalt, 1999), hydroxyl (OH) radical is vital in oxidizing primary pollutants such as volatile organic compounds (VOCs) and contributes to secondary organic aerosol (SOA) and tropospheric ozone (O_3) formation. The OH radical has daytime concentrations of 10^5 to 10^7 molecules cm^{-3} , exhibiting daily (Cao et al., 2020; Tan et al., 2017), seasonal (Friedman and Farmer, 2018), as well as spatial (Cao et al., 2020; Stone et al., 2012) variations. An average daily OH radical concentration of 1.5×10^6 molecules cm^{-3} is widely used to estimate the photochemical age of an air mass (Mao et al., 2009). Typical VOCs have second-order rate constants of 10^{-15} to $10^{-10} \text{ cm}^3 \text{ molecule}^{-1} \text{ s}^{-1}$ with OH radicals (Atkinson and Arey, 2003; Atkinson et al., 2006), which can be translated to atmospheric lifetimes of hours to approximately a year (Seinfeld and Pandis, 2016). This situation poses challenges in laboratory experiments to directly simulate the OH oxidation of VOCs, which is one of the most important chemical processes in the Earth's atmosphere. Smog chambers (Cocker et al., 2001; Hildebrandt et al., 2009; Wang et al., 2014) and oxidation flow reactors (OFRs) (George et al., 2007; Kang et al., 2007; Lambe et al., 2011) have been widely employed to simulate oxidation of VOCs and subsequent SOA formation. For example, the Caltech Chamber provides oxidation conditions close to the real atmosphere, making it suitable for the study of complex multi-step reactions and low-volatility products. However, each experiment takes several hours to days and long-duration experiments are prone to background interference. The Toronto Photo-Oxidation Tube (TPOT) focuses on the study of heterogeneous oxidation reactions of aerosols. Its 0.8 L volume makes it portable, but it is prone to uneven residence time distribution (RTD) and significant wall effects. The Potential Aerosol Mass Oxidation Flow Reactor (PAM-OFR) and the Gothenburg Potential Aerosol Mass Oxidation Flow Reactor (Go: PAM-OFR) are often used to study the transformation of gaseous precursors into particles (such as the formation of SOA). The Go: PAM-OFR has a volume of 7.2 L, which is only half that of the PAM-OFR, making it suitable for experiments on mobile platforms. However, its small volume gives it the same disadvantages as the TPOT, and it is equipped with only a single UV lamp, which does not allow for as wide a range of controllable oxidation levels as the PAM-OFR. The PAM's moderate volume and central flow sampling can reduce wall effects.

67 These OFRs of reactors normally operate with high concentrations of oxidants (e.g., OH radicals), which lead to a significant
 68 acceleration of oxidation reactions, often by orders of magnitude. To reconcile the differences in OH concentration and
 69 exposure time between ambient and laboratory settings, the oxidation extent, i.e., OH exposure (OH_{exp} , molecules cm^{-3} s) is
 70 normally used to extrapolate laboratory findings to ambient conditions. Despite drawbacks such as possible altered reaction
 71 mechanisms, this approach provides a quantitative assessment of the chemistry during OH oxidation in a reasonable time span
 72 and achievable detection capability. The OH_{exp} has a significant impact on the yield and product distribution during VOC
 73 oxidation (Cheng et al., 2021; Cheng et al., 2024). Accurate measurement or estimation of the OH_{exp} during laboratory
 74 experiments, therefore, is the key to understanding the oxidation chemistry that can represent the ambient conditions. In this
 75 study, we chose to further investigate the PAM-OFR to explore its OH_{exp} , as it offers moderate conditions in terms of
 76 experiment time, deployment complexity, range of oxidation levels, and wall effects.

77 The Aerodyne Potential Aerosol Mass OFR (PAM-OFR) is one of the most widely used OFRs for studying SOA formation
 78 and evolution (Zhang et al., 2024). It can achieve a wide range of atmospheric OH_{exp} conditions within short residence times
 79 on the order of minutes (Kang et al., 2007; Lambe et al., 2011). The PAM-OFR can be operated in a number of modes,
 80 depending on 1) the wavelength of the ultraviolet (UV) light source, 2) the concentration of the externally generated O_3 (if
 81 any), and 3) the injection of external precursor to generate NO_x ($= \text{NO} + \text{NO}_2$) or other oxidants (e.g., nitrate radical or halogen
 82 atoms) upon photolysis. The most widely used methods for OH generation include combined photolysis of O_2 and H_2O at $\lambda =$
 83 185 nm plus photolysis of O_3 at $\lambda = 254$ nm (OFR185; R1–R6) or photolysis of externally added O_3 at $\lambda = 254$ nm (OFR254;
 84 R5–R6) (Rowe et al., 2020):



91 To obtain the OH_{exp} under these two modes in the PAM-OFR, one can perform decay experiments on trace gases such as SO_2
 92 and CO , and fit the OH_{exp} based on known second-order rate constants between OH radical and the trace gases, which is
 93 defined as $\text{OH}_{\text{exp, dec}}$. Based on the results of the decay experiments, Li et al. (2015) and Peng et al. (2015) developed estimation
 94 equations to parameterize OH_{exp} as a function of easily measurable quantities, which is denoted as $\text{OH}_{\text{exp, est}}$. A set of parameters
 95 (a – f and x – z , respectively) for the estimation equations of the OFR185 and OFR254 modes (see Sect. 2.3 for details) were
 96 obtained by fitting the estimation equations to $\text{OH}_{\text{exp, dec}}$ values obtained from decay experiments.

97 When using the PAM-OFR in field studies, it is necessary to obtain concurrent OH_{exp} that is representative of the ambient
98 conditions. However, environmental conditions in field studies (e.g., humidity, temperature, etc.) are constantly changing,
99 making it challenging to replicate these conditions for OH_{exp} estimation. In some field studies using PAM-OFR, concurrent
100 OH_{exp} was estimated by measuring the relative decay of benzene and toluene (Liao et al., 2021; Liu et al., 2018). Additionally,
101 some studies have mentioned that OH concentrations can be indirectly measured by detecting the decay of tracers such as 3-
102 pentanol, 3-pentanone, pinonaldehyde, or butanol-d9 (Barmet et al., 2012). However, the measurement of all these organic
103 tracers requires specific, sophisticated instruments such as proton-transfer-reaction time-of-flight mass spectrometers (PTR-
104 MS). Additionally, switching the instrument back and forth between the front and end of the OFR during field measurements
105 can result in some loss of real-time VOCs data before entering the OFR. To obtain accurate OH_{exp} , some studies explicitly
106 modelled the radical chemistry in PAM-OFR (Li et al., 2015; Ono et al., 2014; Peng et al., 2015). The estimation equations
107 developed by Li et al. (2015) and Peng et al. (2015), although empirical, reproduced the OH_{exp} from models within 10 %,
108 making them a good choice because these equations only require the input of a few easily available parameters. Yet, it is
109 unclear whether the fitted parameters obtained under certain conditions can still accurately estimate OH_{exp} when experimental
110 conditions, such as UV light intensity, water vapor mixing ratio, residence time, and external OH reactivity (OHR_{ext}), undergo
111 significant changes. Furthermore, there is currently no consensus on the minimum number of decay experiments required to
112 obtain accurate parameterization for OH_{exp} estimation using these equations. This facet is important for field studies using
113 PAM-OFR where only limited numbers of decay experiments can be done to obtain concurrent OH_{exp} estimation.
114 In this study, we conducted a series of experiments using the decay of SO_2 and CO to estimate the OH_{exp} in the PAM-OFR
115 under OFR185 and OFR254 modes. The applicability of previously developed OH_{exp} estimation equations to obtain accurate
116 OH_{exp} in the PAM-OFR has been evaluated by linear regression of $\text{OH}_{\text{exp, est}}$ against $\text{OH}_{\text{exp, dec}}$. We have also evaluated how
117 well estimation equations perform when using limited ranges of experimental parameters (e.g., OHR_{ext} , residence time, water
118 mixing ratio, etc.) or different trace gases (SO_2 and CO) and given recommendations. In addition, we have proposed the
119 minimal number of trace-gas decay experiments required to obtain a set of usable parameters for the OH_{exp} estimation
120 equations. Finally, we also compared the advantages and disadvantages of the OFR185 and the OFR254 modes from the
121 perspective of the quantification of OH_{exp} . The methodology of this study can be applied to laboratory and field experiments
122 for OH_{exp} estimation using PAM-OFR or other OFRs that follow a plug-flow assumption.

123 2 Methods

124 2.1 The PAM-OFR

125 Experiments were conducted using an Aerodyne PAM-OFR (Aerodyne Research Inc., Billerica, MA, US), which is a
126 horizontal aluminium cylindrical chamber with an internal volume of 13.3 L. The PAM-OFR operates in a continuous flow
127 mode. Four low-pressure Hg lamps are installed inside the reactor to produce UV light with characteristic spectral lines (e.g.,
128 185 and 254 nm). The OH is generated via OFR185 using two ozone-producing Hg lamps (GPH436T5VH/4P, Light Sources,

Inc.) or via OFR254 using two ozone-free Hg lamps (GPH436T5L/4P, Light Sources, Inc.) to photolyze externally added ozone. A flow of nitrogen purge gas, ranging from 0.2 to 0.3 L min⁻¹, is introduced between the lamps and sleeves. This nitrogen gas flow serves to reduce the heat generated by the lamps and prevent the formation and accumulation of ozone between the lamps and the quartz tubes that isolate them from the sample flow in the OFR. A fluorescent dimming ballast is used to control the photon flux by regulating the voltage applied to the lamps, which allows us to generate different OH concentrations. In typical measurement sequences, nine lamp voltage settings (including lights off) were cycled through every 2–3 hours. The dimming voltage ranged from 0 to 10 V direct current (DC).

2.2 OH_{exp} estimation through decay of SO₂ and CO (OH_{exp, dec})

OH_{exp} can be indirectly measured by detecting the decay of the tracers with known reaction rates. Inorganic trace gases SO₂ or CO react with OH radicals at slower rates compared to most VOCs. However, considering the complex oxidation chemistry of VOCs, SO₂ and CO can better capture the features of real OHR_{ext} decay and effective OHR_{ext} (Peng et al., 2015). We performed systematic decay experiments with SO₂ and CO in the PAM-OFR, with conditions tabulated in Tables S1 and S2. Figure S1 shows the schematics of the experimental setups in the OFR185 and OFR254 modes. In the OFR185 mode, the injected gas flow at the inlet of the PAM is made up of three sub-flows: (1) The trace-gas flow, i.e. SO₂ of 0.2–8.7 ppm or CO of 10.2–207.5 ppm supplied from gas cylinders (Purity: 99.9 % of SO₂, 99.95 % of CO; Shanghai Shenkai Gases Technology CO., LTD.); (2) dry clean air from a zero-air generator (ZAS-100/150, Convenient) with a non-methane hydrocarbon content of less than 1 ppb; (3) the humidified clean air passed through a Nafion humidifier (FC100-80-6MSS, Perma Pure). By adjusting the ratio of dry air to humidified air, the water vapor mixing ratio in the PAM-OFR can be controlled. Additionally, they also serve as makeup flows to maintain a constant flow rate. At the outlet of the reactor, the gas flow was sampled from an internal perforated Teflon ring. The gas-phase species (O₃, SO₂, and CO) were detected using an ultraviolet ozone analyser (UV-100, Eco Sensors), an SO₂ monitor (Model 43i, Thermo Scientific), and a CO monitor (G2401, Picarro), respectively. In the OFR254 mode, in addition to the previously mentioned setup, externally generated O₃ (through UV photolysis) with desired concentrations was injected at the inlet of the PAM-OFR.

Figures S2a and S2b depict examples of set and measured parameters during experiments conducted in the OFR185 and OFR254 modes, respectively. In the OFR185 mode, without radical generation to oxidize the tracer species, their concentration was allowed to stabilize under dark conditions. Once the concentration reached a steady state, the UV lamps were turned on. Different light intensities lead to varying levels of decay of SO₂ or CO after oxidation, reflecting different OH_{exp} within the PAM-OFR. In the OFR254 mode, it is necessary to obtain the initial concentration of O₃ injected into the PAM-OFR in the absence of OHR_{ext}. While waiting for the SO₂ or CO concentration to stabilize, the O₃ flow was temporarily blocked outside the PAM-OFR using a valve. Dry clean air was then introduced to compensate for this portion of the flow, ensuring a constant total flow throughout the entire process. Once the tracer species concentration had reached a steady state, the O₃ was then allowed to flow into the PAM-OFR. The total OH_{exp, dec} in the reactor was varied over a wide range (approximately 10⁹–10¹² molecules cm⁻³ s) by changing the UV light intensity, water mixing ratio, and residence time. The mean residence time was

obtained from the ratio of the internal volume of and the total flow rate through the PAM-OFR. In the calculation of $\text{OH}_{\text{exp, dec}}$ (see the paragraph below), plug flow conditions were assumed, which has been shown to agree with the RTD approach for OH_{exp} when using species (such as SO_2 or CO) with low reaction rate constants with OH radicals ($k_{i, \text{OH}}$) by Li et al. (2015) and Peng et al. (2015). $\text{OH}_{\text{exp, dec}}$ in the PAM-OFR was calculated from the pseudo-first-order reaction of OH with SO_2 or CO , whose $k_{i, \text{OH}}$ have been well characterized ($k_{\text{SO}_2, \text{OH}} = 9.49 \times 10^{-13} \text{ cm}^3 \text{ molecule}^{-1} \text{ s}^{-1}$ and $k_{\text{CO}, \text{OH}} = 2.4 \times 10^{-13} \text{ cm}^3 \text{ molecule}^{-1} \text{ s}^{-1}$ at 1 atm and 298 K) (Burkholder et al., 2020; Cao et al., 2020). By measuring the decay of SO_2 or CO , the corresponding $\text{OH}_{\text{exp, dec}}$ is calculated as follows:

$$\text{OH}_{\text{exp, dec}} = \frac{-1}{k_{i, \text{OH}}} \times \ln \left(\frac{c_{i, \text{out}}}{c_{i, \text{in}}} \right) \quad (1)$$

where $c_{i, \text{in}}$ is the concentration of reactant i injected into the PAM-OFR (ppb), $c_{i, \text{out}}$ is reactant i concentration at the PAM-OFR outlet (ppb), and $k_{i, \text{OH}}$ is the second-order rate constant between the trace species (SO_2 or CO) and OH radicals.

2.3 OH_{exp} estimation from empirical equations ($\text{OH}_{\text{exp, est}}$)

Li et al. (2015) proposed an $\text{OH}_{\text{exp, est}}$ estimation equation (Eq. 2) for OFR185 based on easily measurable quantities:

$$\text{OH}_{\text{exp, est}} = 10^{[a + (b + c \times \text{OHR}_{\text{ext}}^d + e \times \log(\text{O}_{3, \text{out}} \times \frac{180}{t}) \times \text{OHR}_{\text{ext}}^f) \times \log(\text{O}_{3, \text{out}} \times \frac{180}{t}) + \log \text{H}_2\text{O} + \log(\frac{t}{180})]} \quad (2)$$

where $a-f$ are fitting parameters (values are reported in Table S5); $\text{O}_{3, \text{out}}$ is ozone concentration measured at the exit of the PAM-OFR (molecules cm^{-3}), which serves as a surrogate for UV flux; H_2O is water vapor mixing ratio in PAM-OFR (%), which is influenced by both temperature and relative humidity; t is mean residence time (s). The total external OH reactivity is represented by $\text{OHR}_{\text{ext}} (\text{s}^{-1}) = \sum_i k_i [C_i]$, where k_i and $[C_i]$ are the rate constants with OH and the concentration of the OH-consuming reactant i in the system (Wang et al., 2020).

Peng et al. (2015) proposed another equation (Eq. (3)) for $\text{OH}_{\text{exp, est}}$ in OFR254:

$$\text{OH}_{\text{exp, est}} = 10^{[x + \log(-\log r_{\text{O}_3}) + y \times (\frac{\text{OHR}_{\text{ext}}}{\text{O}_{3, \text{in}}})^z]} \quad (3)$$

where $x-z$ are fitting parameters (values are reported in Table S6); $\log r_{\text{O}_3}$ ($\log(\text{O}_{3, \text{out}}/\text{O}_{3, \text{in}})$) is the logarithm of the ratio between the output and input O_3 concentrations, which serves as a surrogate for UV flux and also captures the effect of H_2O ; $\text{O}_{3, \text{in}}$ is the concentration of externally injected O_3 into the PAM-OFR (molecules cm^{-3}).

We have performed in total of 62 sets of trace-gas decay experiments with 416 data points for the $\text{OH}_{\text{exp, dec}}$, with 25 sets and 175 data points in the OFR185 mode and 37 sets and 241 data points in the OFR254 mode. In OFR185 mode, the 175 experiments cover an $\text{OH}_{\text{exp, dec}}$ range of $3.57 \times 10^8 - 5.52 \times 10^{12} \text{ molecules cm}^{-3} \text{ s}$, with an equivalent photochemical age ranging from 4 minutes to 43 days. In OFR254 mode, the 241 experiments cover an $\text{OH}_{\text{exp, dec}}$ range of $1.01 \times 10^9 - 2.18 \times 10^{12} \text{ molecules cm}^{-3} \text{ s}$, with an equivalent photochemical age ranging from 11 minutes to 17 days. The error in $\text{OH}_{\text{exp, dec}}$ is derived from the

191 measurement error of the tracer gas, propagated through Eq. 1. When $\text{OH}_{\text{exp, dec}}$ ranged from 3.6×10^8 – 5.5×10^{12} molecules
 192 $\text{cm}^{-3} \text{ s}$, the resulting error values were 1.9×10^8 – 2.4×10^{10} molecules $\text{cm}^{-3} \text{ s}$.
 193 After obtaining the $\text{OH}_{\text{exp, dec}}$ values, we used Eqs. 2 and 3 to fit the parameters a – f and x – z for OFR185 and OFR254 modes,
 194 respectively, given that the experimental parameters such as OHR_{ext} , $\text{O}_{3, \text{out}}$, H_2O , and t (in Eq. 2), and r_{O_3} , OHR_{ext} , and $\text{O}_{3, \text{in}}$
 195 (in Eq. 3) are known. The $\text{OH}_{\text{exp, est}}$ values were then reconstructed with the fitted parameters and the experimental parameters,
 196 and compared with the $\text{OH}_{\text{exp, dec}}$ values via linear regression analysis. Similarly, the error values for all $\text{OH}_{\text{exp, est}}$ values are at
 197 least one order of magnitude smaller than the respective $\text{OH}_{\text{exp, est}}$ values. The generation of OH radicals in PAM-OFR is related
 198 to the photon fluxes at $\lambda = 185 \text{ nm}$ (I_{185}) and $\lambda = 254 \text{ nm}$ (I_{254}). According to Rowe et al. (2020), $I_{185}:I_{254}$ is specific to the Hg
 199 lamp utilized. Since the OH_{exp} estimation equation for OFR185 uses O_3 concentration as a measurable surrogate for the UV
 200 flux at 185 nm, it is also lamp-specific. Because the UV lamps used in our study are different from the BHK lamps employed
 201 by Li et al. (2015), we anticipate that the parameters a – f fitted from our decay experiments (Table S5) should be quite different
 202 from those in Li et al. (2015), which is indeed the case. Similarly, fitting parameters x – z for OFR254 mode from our decay
 203 experiments (Table S6) are also different from those in Peng et al. (2015).

204 3 Results and Discussion

205 3.1 The OFR185 mode: OHR_{ext} level relevant to ambient conditions

206 Field studies showed that the environmental OHR_{ext} mainly fluctuated between 10–30 s^{-1} (Fuchs et al., 2017; Lou et al., 2010;
 207 Lu et al., 2010; Tan et al., 2018; Yang et al., 2017). To investigate the factors that potentially affect the fitting parameters of
 208 Eq. 2 in the estimation of OH_{exp} under ambient conditions, we first performed 16 sets of experiments with OHR_{ext} of 4–23 s^{-1}
 209 using SO_2 as the OHR_{ext} source. With the measured $\text{OH}_{\text{exp, dec}}$, the parameters (a – f) were first derived, which were used to
 210 reconstruct $\text{OH}_{\text{exp, est}}$ using Eq. 2 with known OHR_{ext} , ozone concentration ($\text{O}_{3, \text{out}}$), water vapor mixing ratio (H_2O), and
 211 residence time (t). The reconstructed $\text{OH}_{\text{exp, est}}$ values were plotted against the $\text{OH}_{\text{exp, dec}}$ values calculated from the trace-gas
 212 decay experiments, as shown in Figure 1. The 1:2 and 2:1 lines indicate approximately half an order of magnitude difference
 213 between $\text{OH}_{\text{exp, dec}}$ and $\text{OH}_{\text{exp, est}}$, which is considered to be acceptable as an uncertainty in OH_{exp} estimation.

214 We first investigated the effect of changing residence time on the OH_{exp} estimation. With other experimental parameters (i.e.
 215 H_2O , $\text{O}_{3, \text{out}}$, and OHR_{ext}) being similar, we set the residence time to a low value (33 s) and also a range of higher values (61–
 216 200 s). The detailed ranges of each experimental condition for different datasets are listed in Table S3. With the residence time
 217 of 33 s, the reconstructed $\text{OH}_{\text{exp, est}}$ correlates well with the experimental $\text{OH}_{\text{exp, dec}}$ (slope = 1.061 and $R^2 = 0.990$, Figure 1a1).
 218 The set of fitted parameters a – f ($\text{FP}_{\text{st, 185}}$; st: short time) applied in Figure 1a1 is presented in Table S5. When the residence
 219 time was increased to 61–200 s, the interpolated $\text{OH}_{\text{exp, est}}$ utilizing $\text{FP}_{\text{st, 185}}$ was also in good correlation with $\text{OH}_{\text{exp, dec}}$ (slope
 220 = 0.978, $R^2 = 0.959$, Figure 1a2). We also derived fitted parameters ($\text{FP}_{\text{et, 185}}$; et: extended t) using the data points with the
 221 extended range of residence time (33–200 s). Not surprisingly, with the application of $\text{FP}_{\text{et, 185}}$, $\text{OH}_{\text{exp, est}}$ also correlated well
 222 with $\text{OH}_{\text{exp, dec}}$ (slope = 0.994, $R^2 = 0.955$, Figure 1a3). The results indicate that variation in residence time does not significantly

223 affect the fitting parameters of Eq. 2 for the OH_{exp} estimation. From an experimental perspective, since OH_{exp} is the product
 224 of OH radical concentration ($[\text{OH}]$) and the residence time (t), as long as the change of t does not significantly alter the quasi-
 225 steady-state $[\text{OH}]$, the fitted parameters from a narrow range of t should be applicable to situations of longer t . Mathematically,
 226 two terms of $180/t$ and $t/180$ are related to t , ranging from 0.90–5.45 and 0.18 to 1.11, respectively, which do not contribute
 227 significantly to the exponent in Eq. 2 after taking the logarithm of them. It is important to note that the above discussion
 228 regarding residence time assumes a plug-flow condition within the PAM-OFR, which is applicable to substances with low k_i
 229 OH , such as SO_2 (or CO). For species that react rapidly with OH, such as monoterpenes or toluene, localized concentration
 230 gradients can develop within the OFR, leading to a significant uneven actual RTD that affects the estimation of OH_{exp} (Palm
 231 et al., 2018).

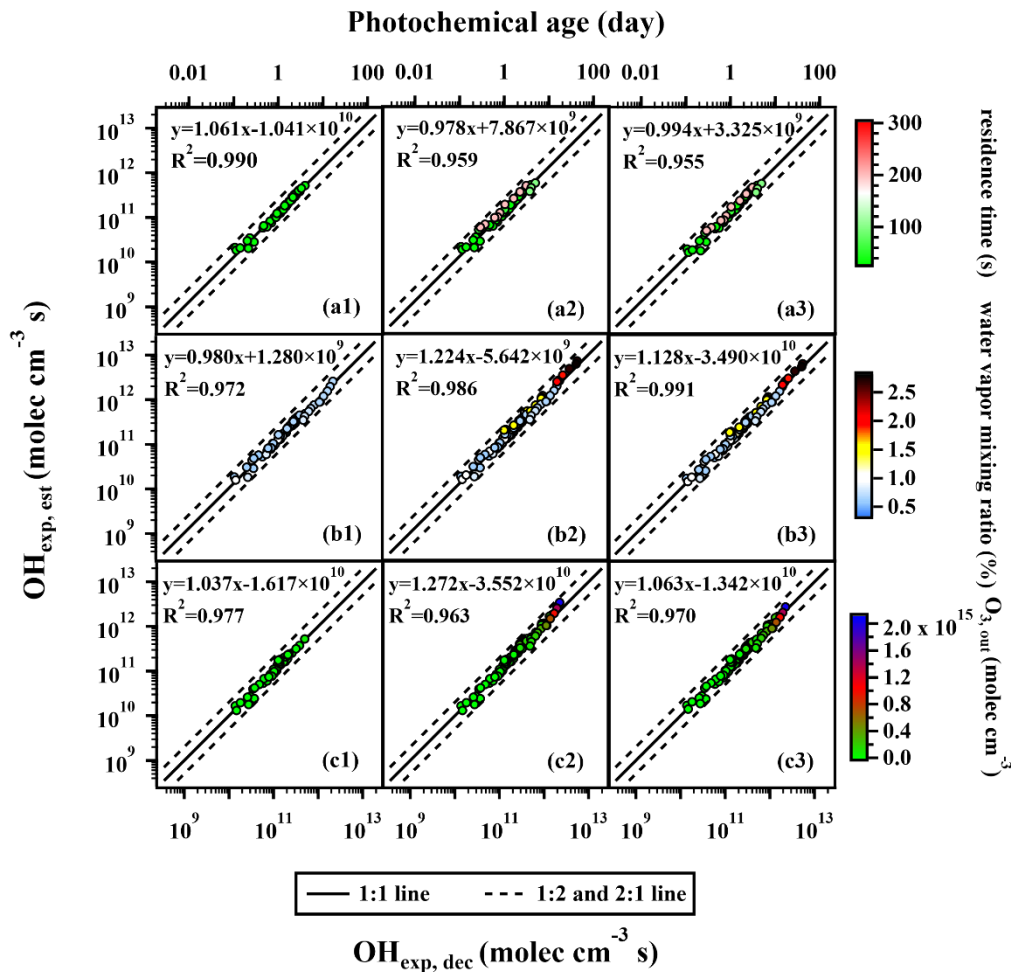
232 Similarly, we then investigated the impacts of H_2O on the estimation of OH_{exp} . Applying fitted parameters from experiments
 233 of low water vapor mixing ratios (0.49–0.99 %, Figure 1b1) ($\text{FP}_{\text{IH}_2\text{O}, 185}$; IH_2O : low H_2O) to data spanning a wide range of
 234 water vapor mixing ratios (0.49–2.76 %) also yielded a reasonably good correlation between $\text{OH}_{\text{exp, est}}$ and $\text{OH}_{\text{exp, dec}}$ (Figure
 235 1b2). This could be attributed to the fact that the term $\log\text{H}_2\text{O}$ in Eq. 2 does not contribute significantly to the exponent.

236 As for ozone concentration, applying fitting parameters ($\text{FP}_{\text{IO}_3, 185}$; IO_3 : low $\text{O}_{3, \text{out}}$) from experiments of low ozone
 237 concentration (1.44×10^{12} – 6.79×10^{13} molecules cm^{-3} , Figure 1c1) to reconstruct the data for a wide range (1.44×10^{12} – 2.03
 238 $\times 10^{15}$ molecules cm^{-3}) yielded a reasonably good correlation between $\text{OH}_{\text{exp, est}}$ and $\text{OH}_{\text{exp, dec}}$ (Figure 1c2). It only resulted in
 239 a mildly increased slope (from 1.063 to 1.272) and similar R^2 values (both are 0.970) as compared to those using the whole
 240 ozone concentration range (Figure 1c3).

241 Ideally, trace-gas decay experiments covering the entire ranges of the t , H_2O , and $\text{O}_{3, \text{out}}$ variations under real experimental
 242 conditions should be conducted, which is labor-intensive. Practically, due to the atmospherically relevant variations that occur
 243 in t , H_2O , and $\text{O}_{3, \text{out}}$ during the real experiments, the ranges of t , H_2O , and $\text{O}_{3, \text{out}}$ covered by trace-gas decay experiments are
 244 usually narrower compared to the real experiments. Our results suggest that the fitting parameters (a – f) obtained from
 245 calibration experiments with relatively narrow ranges of t , H_2O , and $\text{O}_{3, \text{out}}$ can still provide a reliable estimation of OH radical
 246 levels during the real experiments, which would cover wider ranges of these conditions.

247 It is noteworthy that reliable estimations can be achieved regardless of whether the narrow range is situated within the lower
 248 or higher interval of the full condition range. Figure 1 demonstrated the case where the narrow range was situated within the
 249 lower interval, while Figure S3 presented the case where the narrow range was situated within the higher interval. The detailed
 250 ranges of each experimental condition for different datasets are listed in Table S3. As shown in Figure S3, the data points in
 251 panel a1 had residence times of 100–296 s, the data points in panel b1 had water vapor mixing ratios of 1.04–2.76 %, and the
 252 data points in panel c1 had $\text{O}_{3, \text{out}}$ of 8.45×10^{13} – 2.03×10^{15} molecules cm^{-3} . Panels a2, b2, and c2 built on panels a1, b1, and
 253 c1 by incorporating data points with shorter t (33–61 s), lower H_2O (0.49–0.97 %), and lower $\text{O}_{3, \text{out}}$ (1.44×10^{12} – 6.79×10^{13}
 254 molecules cm^{-3}), respectively, but still used fitting parameters a – f obtained from the higher range of conditions to estimate
 255 $\text{OH}_{\text{exp, est}}$. In panels a3, b3, and c3, the parameters a – f were refitted using all the data points included in the expanded t , H_2O ,
 256 and $\text{O}_{3, \text{out}}$ ranges, respectively, and the obtained a – f were used to estimate $\text{OH}_{\text{exp, est}}$. Using panel a1–a3 in Figure S3 as an

example, the slope and R^2 values in a2 and a3 were very close to 1, reflecting the good consistency between $\text{OH}_{\text{exp, est}}$ and $\text{OH}_{\text{exp, dec}}$. In the OFR254 mode discussed later (Figure 4, panels c1–c3), this narrower range can also be situated within the middle interval of the full condition range. This applicability of fitting parameters obtained from narrow ranges of experimental conditions is beneficial for quickly obtaining concurrent OH_{exp} during the experiments in field measurements.



261

Figure 1: The regression results of $\text{OH}_{\text{exp, est}}$ and $\text{OH}_{\text{exp, dec}}$ when variations occurred in (a1–a3) residence time, (b1–b3) water vapor mixing ratio, and (c1–c3) output O₃ concentration under atmospheric relevant OHR_{ext} level (4–23 s⁻¹). Compared to panels a1, b1, and c1, panels a2, b2, and c2 respectively incorporated additional data points with higher t , H₂O, and O_{3, out} values, but still utilized the fitting parameters $\text{FP}_{\text{st}, 185}$, $\text{FP}_{\text{H}_2\text{O}, 185}$, and $\text{FP}_{\text{O}_3, 185}$ obtained from the lower condition range to estimate $\text{OH}_{\text{exp, est}}$. In panels a3, b3, and c3, all data points within the extended condition range were used to re-fit the parameters a – f , and the resulting $\text{FP}_{\text{et}, 185}$, $\text{FP}_{\text{eH}_2\text{O}, 185}$, and $\text{FP}_{\text{eO}_3, 185}$ were employed to estimate $\text{OH}_{\text{exp, est}}$ (s: short, l: low, e: extended).

3.2 The OFR185 mode: OHR_{ext} level relevant to emission sources

The experimental conditions in the PAM-OFR often involve not only general atmospheric conditions (OHR_{ext} < 30 s⁻¹) but also high-concentration conditions, e.g., those directly from emission sources. For instance, the OHR_{ext} of direct vehicle

emission can be as high as 1000 s^{-1} with plenty of reducing gases such as CO and VOCs (Nakashima et al., 2010). To evaluate the applicability of Eq. 2 under situations of high OHR_{ext} , we performed high OHR_{ext} (up to 204 s^{-1}) experiments using high concentrations of SO_2 as the OHR_{ext} source. Compared to the data points shown in Figure 2a ($4\text{--}23\text{ s}^{-1}$), Figure 2b and Figure 2c included additional data points with higher OHR_{ext} values ($198\text{--}204\text{ s}^{-1}$), while the other conditions remained similar. In Figure 2b, the parameters $a\text{--}f$ ($\text{FP}_{\text{IOHR}, 185}$; IOHR: low OHR_{ext}) obtained from the low- OHR_{ext} data points were used to estimate $\text{OH}_{\text{exp, est}}$, yet those used in Figure 2c were refitted from the data points with extended OHR_{ext} range ($4\text{--}204\text{ s}^{-1}$). It could be observed from Figure 2b that when estimating OH_{exp} using $\text{FP}_{\text{IOHR}, 185}$, $\text{OH}_{\text{exp, est}}$ of the high- OHR_{ext} data points were significantly overestimated, with a difference of more than two orders of magnitudes compared to $\text{OH}_{\text{exp, dec}}$. This observation suggests that, different from cases for residence time, water vapor mixing ratio, and ozone concentration shown in the section above, $\text{FP}_{\text{IOHR}, 185}$ were not applicable to high- OHR_{ext} conditions.

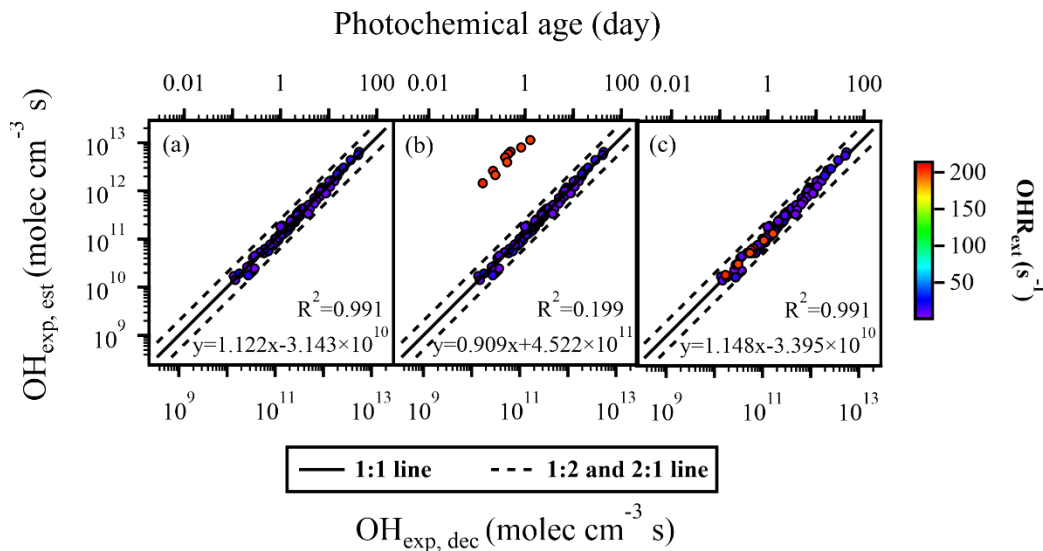
We then investigated the possible causes of the discrepancy for OH_{exp} estimation between $\text{FP}_{\text{IOHR}, 185}$ and $\text{FP}_{\text{eOHR}, 185}$ (eOHR: extended OHR_{ext}). From a mathematical perspective, according to Eq. 2, the third term $c \times \text{OHR}_{\text{ext}}^d \times \log(\text{O}_{3, \text{out}} \times 180/t)$ and the fourth term $e \times \text{OHR}_{\text{ext}}^f \times [\log(\text{O}_{3, \text{out}} \times 180/t)]^2$ are associated with OHR_{ext} , which involve fitted parameters of $c\text{--}f$. To investigate their relationships with OHR_{ext} , we performed a sensitivity test with a fixed ozone concentration ($1.77 \times 10^{14}\text{ molecules cm}^{-3}$) and residence time (89 s), which were mean values during our experiments. When using the $c\text{--}f$ values of $\text{FP}_{\text{IOHR}, 185}$ (-0.13922, 0.26786, 0.0026332, and 0.4917), the variations of the third term, the fourth term, and their sum with respect to OHR_{ext} were shown in Figure S4a1–a3, respectively. The third term (Figure S4a1) was negative and decreased as OHR_{ext} increased, while the fourth term (Figure S4a2) was positive and increased as OHR_{ext} increased. The sum of them (Figure S4a3), however, first decreased and then started to increase at approximately $\text{OHR}_{\text{ext}} = 21\text{ s}^{-1}$, owing possibly to a slower decrease in the third term or a faster increase in the fourth. If contributions from other terms in Eq. 2 were constant, this led to an increase of OH_{exp} as OHR_{ext} increased beyond 21 s^{-1} . Our results showed that the expectation that OH_{exp} should decrease with increasing OHR_{ext} (Li et al., 2015) was applicable to the lower ranges of OHR_{ext} , i.e., under atmospheric relevant conditions. With further increase of OHR_{ext} , i.e., above atmospheric relevant condition, the fitted parameters obtained from the dataset with $\text{FP}_{\text{IOHR}, 185}$ were not applicable.

When using the $c\text{--}f$ values of $\text{FP}_{\text{eOHR}, 185}$ (-0.079114, 0.36805, 0.0041654, and 0.38722), the trends of the third and the fourth terms (Figure S4b1 and S4b2, respectively) were similar to those with low OHR_{ext} (Figure S4a1 and S4a2, respectively); their sum, however, gave a monotonical decreasing trend as OHR_{ext} increased (Figure S4b3), consistent with the expectation that OH_{exp} should decrease with increasing OHR_{ext} (Li et al., 2015). The curve in Figure S4b3 can continue to decrease monotonically at higher OHR_{ext} values, at least until 2000 s^{-1} .

From the perspective of oxidation chemistry, high concentrations of gas phase SO_2 could lead to more SO_2 entering the particle phase. The H_2O_2 in the liquid water of nucleated sulfuric acid aerosols would further oxidize SO_2 (Liu et al., 2020), which could lead to the discrepancy for OH estimation between low OHR and extended high OHR.

Nevertheless, the good agreement between $\text{OH}_{\text{exp, est}}$ and $\text{OH}_{\text{exp, dec}}$ in Figure 2c (using re-fitted parameters from the dataset of extended OHR_{ext}) indicate that Eq. 2 can still be used to estimate OH_{exp} under high- OHR_{ext} conditions. This conclusion is

305 further supported by the results of OH_{exp} obtained using CO as the OHR_{ext} source (see Figure 3 and the section below) under
 306 extremely high- OHR_{ext} conditions (up to 1200 s^{-1}). This is advantageous for the use of PAM-OFR in simulations of SOA
 307 formation from direct emission sources (e.g., vehicular exhaust and biomass burning) where OHR_{ext} is extremely high. It is,
 308 however, desirable to have OH_{exp} estimated under similarly high OHR_{ext} for those experiments to accurately represent the
 309 extent of oxidation.



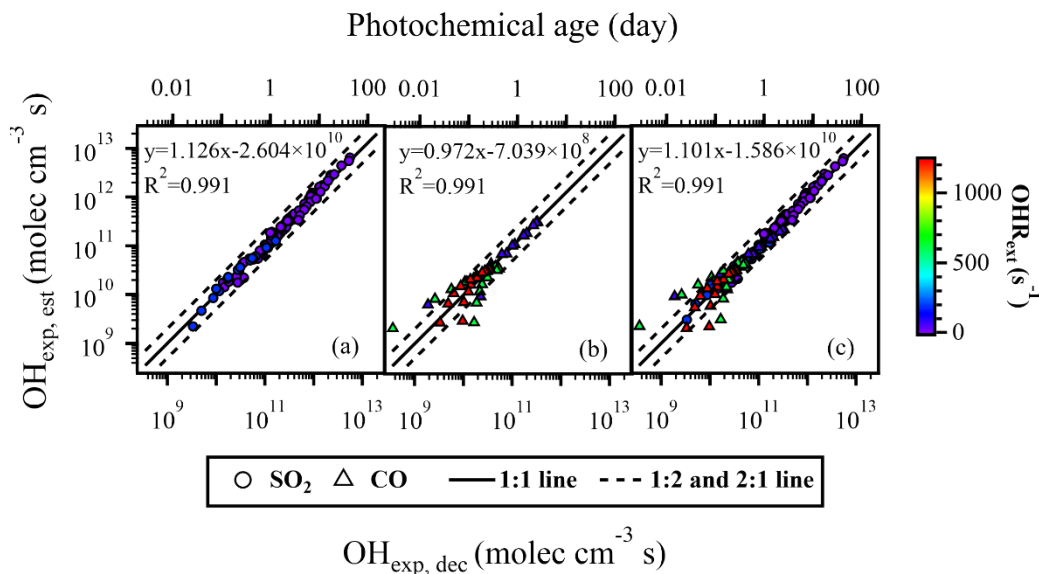
310

311 **Figure 2: The regression results of $\text{OH}_{\text{exp, est}}$ and $\text{OH}_{\text{exp, dec}}$ with different OHR_{ext} levels. In panel a, data points with atmospheric**
 312 **relevant OHR_{ext} level ($4\text{--}22 \text{ s}^{-1}$) were applied. In addition to the data points contained within panel a, panel b included additional**
 313 **data points with emission sources related OHR_{ext} level ($198\text{--}204 \text{ s}^{-1}$), but $\text{FP}_{\text{IOHR, 185}}$ were still used to estimate $\text{OH}_{\text{exp, est}}$. In panel b,**
 314 **data points in red showed that the $\text{OH}_{\text{exp, est}}$ of these high- OHR_{ext} data points were significantly overestimated. $\text{FP}_{\text{IOHR, 185}}$ were not**
 315 **applicable to high- OHR_{ext} conditions. The data points in panel c were identical to those in panel b, but the estimation of $\text{OH}_{\text{exp, est}}$**
 316 **utilized the $\text{FP}_{\text{eOHR, 185}}$ obtained by fitting all data points across the full range of OHR_{ext} levels.**

317 3.3 The OFR185 mode: SO_2 and CO as OHR_{ext} sources

318 Peng et al. (2015) suggested that SO_2 can better capture the features of real OHR_{ext} decay and effective OHR_{ext} . The reaction
 319 between SO_2 and OH is relatively straightforward and is not expected to undergo too many side reactions. CO is a typical
 320 gaseous inorganic compound emitted during combustion process. Using CO as an OHR_{ext} source to explore the estimation of
 321 OH_{exp} in the simulation of oxidation chemistry for emission sources (i.e., high OHR_{ext} level) is representative. Therefore, we
 322 compared the results with SO_2 (Figure 3a) and CO (Figure 3b) as the OHR_{ext} source. When using SO_2 as the OHR_{ext} source,
 323 all data points agreed within a factor of 2 (Figure 3a). while only approximately 83 % of the data points agreed within a factor
 324 of 2 when CO was used as the OHR_{ext} source (Figure 3b). The deviating data points were mostly concentrated in areas with
 325 high OHR_{ext} ($> 600 \text{ s}^{-1}$) and low $\text{O}_{3, \text{out}}$ concentration ($10^{12}\text{--}10^{13} \text{ molecules cm}^{-3}$), where the removal of CO was relatively low.
 326 Li et al. (2015) have observed increased deviations between $\text{OH}_{\text{exp, est}}$ and $\text{OH}_{\text{exp, dec}}$, which was attributed, at least in part, to
 327 the increased measurement uncertainties for CO when the decrease of its concentration was marginal. We believe that

328 measurement uncertainty might not be the main reason in our case, because most of the decreases in CO concentration during
 329 our experiments were larger than the precision of the Picarro G2401 Analyzer (~ 1.5 ppb at 5 min time resolution). Another
 330 possible reason is that in addition to the reaction with OH radicals, CO may react with some other oxidants, leading to its
 331 consumption, while SO₂ was less affected, thereby resulting in more scattered data points for CO. The reaction rate of CO with
 332 HO₂ is very slow, and is unlikely to play a significant role ($k_{\text{CO, HO}_2} = 5.55 \times 10^{-27} \text{ cm}^3 \text{ molecule}^{-1} \text{ s}^{-1}$ at 300 K) (You et al.,
 333 2007). Cohen and Heicklen (1972) suggested that CO could also react with atomic oxygen (O(¹D)). Clerc and Barat (1967)
 334 have reported some appreciable rate coefficients (10^{-11} to $10^{-12} \text{ cm}^3 \text{ molecule}^{-1} \text{ s}^{-1}$) for the reaction between CO and O(¹D),
 335 which are higher than those for the reactions of CO with OH ($k_{\text{CO, OH}} = 2.4 \times 10^{-13} \text{ cm}^3 \text{ molecule}^{-1} \text{ s}^{-1}$ at 298 K) (Burkholder et
 336 al., 2020). It is therefore possible that reaction between CO and O(¹D) might have complicated the decay of CO in the PAM-
 337 OFR. To further investigate this aspect, we used the KinSim, a kinetic simulator, to calculate the average mixing ratios of OH,
 338 O(¹D), and HO₂ under the specific conditions in the PAM-OFR, and then assessed the relative importance of the reactions CO
 339 + OH \rightarrow CO₂ + H, CO + O(¹D) \rightarrow CO₂, and CO + HO₂ \rightarrow CO₂ + OH (Li et al., 2015; Peng and Jimenez, 2019, 2020). The
 340 results show that although the reaction rate constant of CO and O(¹D) is 1–2 orders of magnitude higher than that of CO and
 341 OH, the concentration of OH is about 6–7 orders of magnitude higher than the concentration of O(¹D), indicating that the
 342 reaction of CO with O(¹D) will not have a significant impact on the consumption of CO. The real reason for the scattered data
 343 points when using CO in the trace-gas decay experiment is still unknown.
 344 Figure 3c includes the results of trace-gas decay experiments using both SO₂ and CO as the OHR_{ext} source. Despite having
 345 different reaction rates with OH radicals, the data points could be collectively utilized to fit the parameters for the estimation
 346 equation. With approximately 95 % of the results agreeing within a factor of 2, OH_{exp, est} obtained using the fitted parameters
 347 exhibited good agreements (slope = 1.101, $R^2 = 0.991$) with OH_{exp, dec.} Our results thus suggest that although using CO as the
 348 OHR_{ext} might result in some scattered data points, it was still feasible to use Eq. 2 to estimate OH_{exp} given that experiments
 349 were not done solely in conditions with high OHR_{ext} (i.e., high CO concentrations) and low O₃ concentrations. Another benefit
 350 of using CO as OHR_{ext} source for the estimation of OH_{exp} is that it introduces complexity in the precursor, which resembled
 351 those in real applications. Although not tested in this study, we also note that further trace-gas decay experiments in the
 352 presence of N₂O/NO_x (typical urban environment) should be conducted when oxidation chemistry in the presence of NO_x is
 353 studied (Cheng et al., 2021).



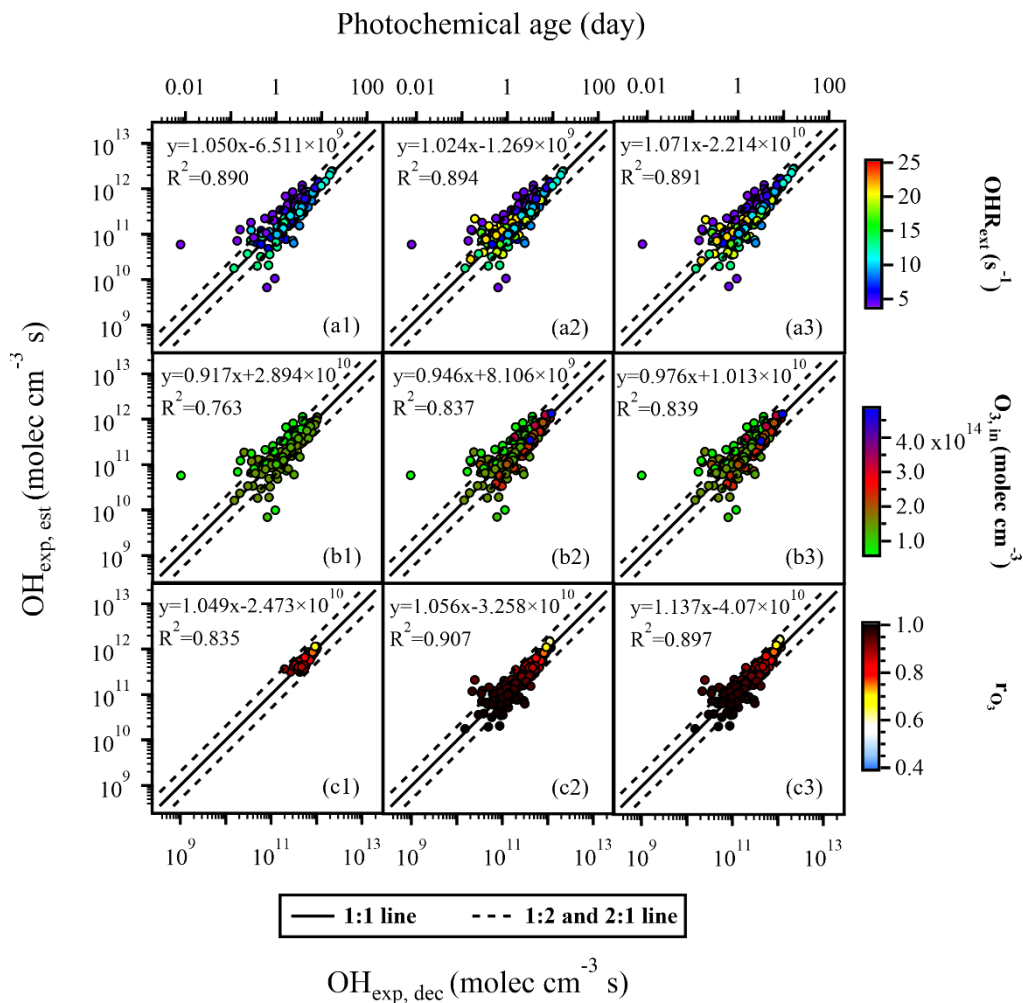
354

355 **Figure 3: The regression results of $\text{OH}_{\text{exp, dec}}$ and $\text{OH}_{\text{exp, est}}$ in the OFR185 mode with (a) SO_2 and (b) CO as OHR_{ext} sources. (c)**
 356 **Results from all experiments (using SO_2 and CO) in the OFR185 mode.**

357 3.4 The OFR254 mode

358 The equation for OH_{exp} estimation in OFR254 mode is simpler compared to that of OFR185 mode. According to Eq. 3, under
 359 OFR254 mode, the three parameters potentially affecting the OH_{exp} are OHR_{ext} , input O_3 concentration, and rO_3 . The detailed
 360 ranges of each experimental condition for different datasets are listed in Table S4. We found that compared to Figure 1, the
 361 data points in Figure 4 were more scattered. Most of the R^2 values in Figure 4 were below 0.9, indicating that using SO_2 as the
 362 OHR_{ext} source, the estimation of OH_{exp} (using Eq. 3) under the OFR254 mode performed not as well as those under the OFR185
 363 mode (using Eq. 2). Firstly, we investigated the impacts of OHR_{ext} . Figure 4a1 showed the regression results of $\text{OH}_{\text{exp, est}}$ and
 364 $\text{OH}_{\text{exp, dec}}$ when OHR_{ext} ranged from 5 to 14 s^{-1} . The parameters $x-z$ ($\text{FP}_{\text{IOHR, 254}}$; IOHR: low external OHR) (Table S6) were
 365 obtained by fitting Eq. 3 to $\text{OH}_{\text{exp, dec}}$. In Figure 4a2, the same set of fitted parameters $\text{FP}_{\text{IOHR, 254}}$ from Figure 4a1 were used for
 366 a wider range of OHR_{ext} (5–21 s^{-1}). From the regression results (slopes of 1.050 and 1.024, R^2 of 0.890 and 0.894), the same
 367 set of parameters yielded similar estimation performance for OH_{exp} despite a wider range of OHR_{ext} in Figure 4a2 compared
 368 to that of Figure 4a1. At the same time, these results were not much different from those (slope = 1.071, $R^2 = 0.891$) using a
 369 re-fitted set of parameters ($\text{FP}_{\text{eOHR, 254}}$; eOHR: extended external OHR) for the wider range of OHR_{ext} (Figure 4a3). Even
 370 though the correlation was not as good as those in the OFR185 mode, approximately 85 % of the data points agreed within a
 371 factor of 2. We did not further extend the OHR_{ext} to values as high as those in the OFR185 mode as discussed above, since the
 372 OFR254 mode was much less oxidative and might not be suitable for simulating the oxidation chemistry of extremely high
 373 OHR_{ext} as those from direct emissions.

374 Similarly good correlations were observed when we only used the fitted parameters ($FP_{IO_3, 254}$ and $FP_{mrO_3, 254}$, respectively; IO_3 :
 375 low $O_{3, in}$, mrO_3 : medium rO_3) from narrow ranges of input O_3 concentration and rO_3 (Figure 4b1 and Figure 4c1, respectively)
 376 to reconstruct the $OH_{exp, est}$ values with extended ranges of these experimental conditions (Figure 4b2 and Figure 4c2,
 377 respectively). Such correlations were as good as those with re-fitted parameters ($FP_{eO_3, 254}$ and $FP_{erO_3, 254}$, respectively; eO_3 :
 378 extended $O_{3, in}$, erO_3 : extended rO_3) from data points in the extended ranges of O_3 concentration and rO_3 (Figure 4b3 and Figure
 379 4c3, respectively). These observations thus indicate that under the OFR254 mode, when OHR_{ext} , $O_{3, in}$, and rO_3 vary within
 380 certain ranges ($5\text{--}21\text{ s}^{-1}$, $6.46 \times 10^{13}\text{--}4.8 \times 10^{14}\text{ molec cm}^{-3}$, and $0.61\text{--}0.99$, respectively), Eq. 3 can be used to estimate
 381 OH radical levels reasonably well using the fitting parameters ($x\text{--}z$) obtained from a narrower range of data points.

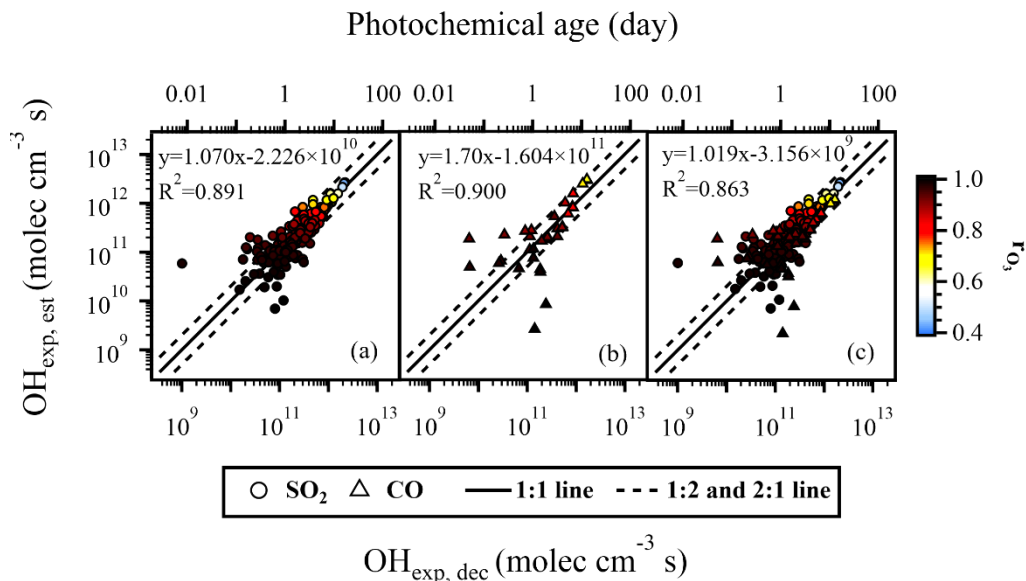


382

383 **Figure 4: The regression results of $OH_{exp, est}$ and $OH_{exp, dec}$ when variations occurred in (a1–a3) OHR_{ext} , (b1–b3) input O_3**
 384 **concentration, and (c1–c3) rO_3 . Compared to panels a1, b1, and c1, panels a2, b2, and c2 respectively incorporated additional data**
 385 **points with extended OHR_{ext} , $O_{3, in}$, and rO_3 values, but still utilized the fitting parameters $FP_{IOHR, 254}$, $FP_{IO_3, 254}$, and $FP_{mrO_3, 254}$**
 386 **obtained from the lower or medium condition range to estimate $OH_{exp, est}$. In panels a3, b3, and c3, all data points within the extended**

387 condition range were used to re-fit the parameters $x-z$, and the resulting $FP_{eOHR, 254}$, $FP_{eO_3, 254}$, and $FP_{eO_3, 254}$ were employed to
 388 estimate $OH_{exp, est}$.

389 Figure 5a and Figure 5b depicted the correlation between $OH_{exp, est}$ estimated from Eq. 3 and $OH_{exp, dec}$ calculated from Eq. 1
 390 with SO_2 and CO as OHR_{ext} sources, respectively. When using SO_2 as the OHR_{ext} source, approximately 86 % of the data
 391 points agreed within a factor of 2 (Figure 5a). Similar to the case of OFR185, when CO was used as the OHR_{ext} source, the
 392 data points were more scattered, with the percentage of data points within a factor of 2 dropping to only about 64 % (Figure
 393 5b). Figure 5c included data points using both SO_2 and CO as the OHR_{ext} sources. Overall, regardless of the OHR_{ext} source,
 394 when r_{O_3} was higher than 0.93, which meant a low UV intensity, the majority of data points for $OH_{exp, est}$ and $OH_{exp, dec}$ differed
 395 by a factor of two or more. It is therefore recommended that when using the OFR254 mode, too low lamp power settings, for
 396 example, UV lamp voltage below 1.5V should be avoided in the case of our study.

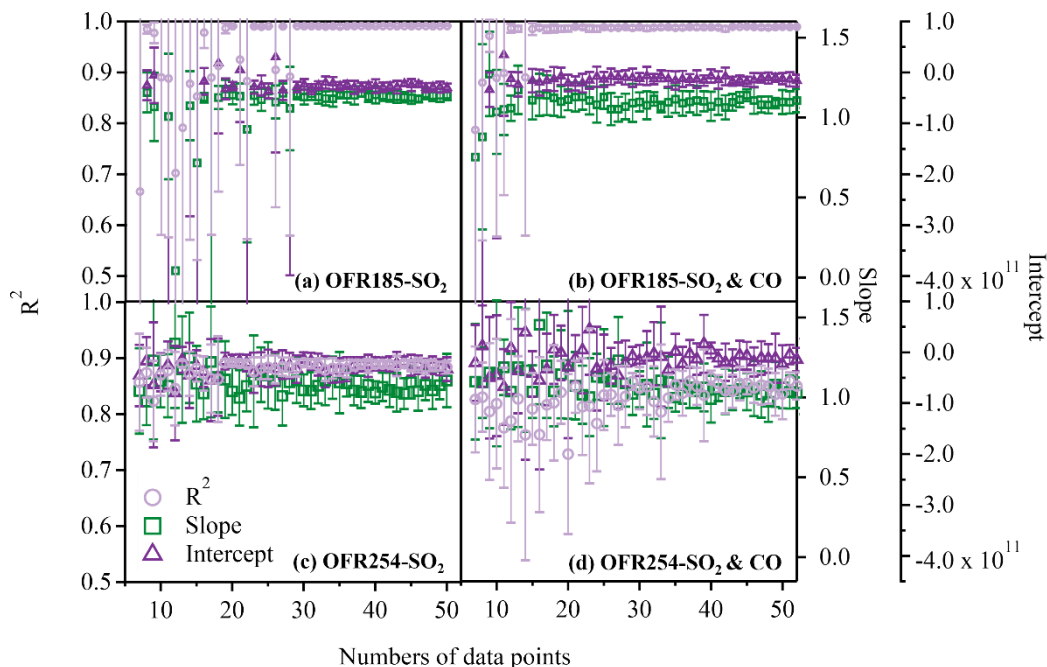


397
 398 **Figure 5: The regression results of $OH_{exp, dec}$ and $OH_{exp, est}$ in the OFR254 mode with (a) SO_2 and (b) CO as OHR_{ext} sources. (c)**
 399 **Results from all experiments (SO_2 and CO) in the OFR254 mode.**

400 4 Conclusions

401 A series of OH_{exp} estimation experiments using the PAM-OFR were conducted in OFR185 and OFR254 modes to explore the
 402 applicability of the empirical equations under a wide range of conditions. The results indicate that for OFR185 mode, when
 403 varying the residence time, water vapor mixing ratio, and output O_3 concentration (as a surrogate for UV intensity) within
 404 certain ranges, the empirical equation (Eq. 2) for OH_{exp} proves to be effective in estimating OH_{exp} . Unless there is a significant
 405 change in OHR_{ext} , such as transitioning from ambient conditions to emission source conditions, there is no need to re-fit the
 406 parameters $a-f$ in the estimation equation to estimate OH_{exp} . Compared with OFR254 mode, the consistency between $OH_{exp, est}$
 407 and $OH_{exp, dec}$ in OFR185 mode is better. For the OFR254 mode, when OHR_{ext} , input O_3 concentration, and r_{O_3} vary within

408 certain ranges, the empirical equation (Eq. 3) can be used to estimate OH_{exp} reasonably well using the parameters $x-z$ obtained
 409 from a narrower range of data points. It is important to note that for the OFR185 mode, the above conclusions are valid only
 410 if one already has a set of $a-f$ values that are appropriate for the specific UV lamps being used, as the $I_{185}:I_{254}$ that affects the
 411 OH_{exp} is lamp-specific. For a PAM-OFR that employs a different Hg lamp, a series of calibration experiments should be
 412 conducted in any case. Alternatively, based on the research by Rowe et al. (2020), the exponential relationship between the $a-$
 413 f values and the $I_{185}:I_{254}$ could be used to first obtain a set of $a-f$ values suitable for the UV lamps being used.
 414 To obtain reliable estimates of OH_{exp} using Eqs. 2 and 3 for the OFR185 mode or OFR254 mode, respectively, it is desirable
 415 to have sufficient data points (that is, $\text{OH}_{\text{exp, dec}}$ from trace-gas decay experiments) to fit the parameters for the calculation of
 416 $\text{OH}_{\text{exp, est}}$. There is currently no consensus on how many data points in trace-gas decay experiments are enough for reliable
 417 fitted parameters, which could be important for in-situ OH_{exp} estimation in field studies where a limited number of experiments
 418 are done to reduce downtime. We aim to address this by random sampling from the data points in our experiments and
 419 determine the minimum number of experiments that are needed to obtain reliable OH_{exp} .
 420 For OFR185 mode, we first used randomly selected N data points from the 175 data points presented previously to fit the
 421 parameters ($a-f$) using Eq. 2. The fitted parameters were then used to reconstruct $\text{OH}_{\text{exp, est}}$ for all the 175 data points. The
 422 $\text{OH}_{\text{exp, est}}$ values were then compared with the corresponding 175 $\text{OH}_{\text{exp, dec}}$ values. This procedure was repeated 10 times for
 423 each N , with N starting from 7 till approximately 50 (Figure 6a). The average R^2 , slope, and intercept from the 10 attempts
 424 were then shown as a function of N for experiments with SO_2 only (Figure 6a) and those with SO_2 and CO (Figure 6b). It can
 425 be observed that around 30 data points are needed for experiments with SO_2 only while around 20 data points are needed to
 426 have stable R^2 values and slopes when using both SO_2 and CO. For OFR254 mode, the same procedure was applied to the 241
 427 data points. It was not surprising that the results were a lot more scattered (Figure 6c and Figure 6d) compared to those for
 428 OFR185 mode given their performance shown in the previous section. Nevertheless, our analysis suggests that around 25 data
 429 points are needed to obtain reliable $\text{OH}_{\text{exp, est}}$ for OFR254 mode, whether SO_2 alone (Figure 6c) or SO_2 and CO (Figure 6d) are
 430 used for the trace-gas decay experiments. Therefore, despite the limitation that this practice only randomly samples the data
 431 points without considering the range of any experimental conditions, our analysis suggests that 20–30 data points are normally
 432 needed to obtain reliable OH_{exp} for both OFR185 and OFR254 modes.



433

434 **Figure 6: The regression results of $\text{OH}_{\text{exp, dec}}$ and $\text{OH}_{\text{exp, est}}$ (characterized by the R^2 , slope, and intercept) when different numbers of**
 435 **data points were chosen. (a) SO₂ as OHR_{ext} source in OFR185 mode, (b) SO₂ or CO as OHR_{ext} source in OFR185 mode, (c) SO₂ as**
 436 **OHR_{ext} source in the OFR254 mode, and (d) SO₂ or CO as OHR_{ext} source in the OFR254 mode.**

437 Our study suggests that the $\text{OH}_{\text{exp, est}}$ estimated from the empirical equations agrees better with $\text{OH}_{\text{exp, dec}}$ for the OFR185
 438 (Figure 3) than for the OFR254 mode (Figure 5). This can be understood from the perspective of OH generation and its
 439 consumption by OHR_{ext} (Li et al., 2015). For the OFR185 mode, there are two pathways to generate OH radicals: the photolysis
 440 of H₂O and the photolysis of O₃. For the OFR254 mode, the main pathway for OH radical generation is solely the photolysis
 441 of O₃. Consequently, when OHR_{ext} changes, the disruption to OH_{exp} in the system is more significant in the case of the OFR254
 442 mode, while the OH_{exp} in the OFR185 mode remains more stable. In addition, pseudo-first-order kinetics between OH radicals
 443 and SO₂ or CO is assumed, with [OH] being at a pseudo-steady state. Yet, the relatively low OH radical generation capacity
 444 in the OFR254 mode might not necessarily always fulfil such an assumption, leading to higher uncertainties for estimating
 445 OH_{exp} . Therefore, the OFR185 mode offers certain advantages such as relatively high OH_{exp} , more accurate OH_{exp} estimation,
 446 as well as no external input of O₃ needed. However, for substances that exhibit strong absorption at the wavelength of 185 nm
 447 and are prone to photolysis, such as aromatic species (Peng et al., 2016), using the OFR254 mode is a better choice. For users
 448 of other OFRs (non-PAM-OFR) who would like to apply the conclusions above, at least two conditions must be met: (1) the
 449 concentration of [OH] within the OFR should remain stable, and (2) the assumption of plug flow conditions is acceptable,
 450 allowing for the neglect of differences in the actual RTD, heterogeneity in the UV light intensity and the concentration of

451 radicals/oxidants at different points within the reactor, which are caused by different designs of reactors (such as wall materials,
452 shapes, or volumes).

453 **Data availability**

454 The data shown in the paper are available on request from the corresponding authors (huangdd@saes.sh.cn and
455 yongjieli@um.edu.mo).

456 **Supplement link**

457 The supplement related to this article is available online at:

458 **Author contribution**

459 QL, DDH, and YJL conceived and planned the experiments. QL and YW carried out the experiments. QL, DDH, and YJL
460 analysed the data and took the lead in writing the paper. QL, DDH, YJL, ATL, and XC contributed to the interpretation of the
461 results. SL, LZ, CYH, ST, QC, KIH, HW, KMM, and CH provided significant input during the revision of the manuscript. All
462 authors provided feedback on the paper.

463 **Competing interests**

464 The authors declare no competing interests.

465 **Acknowledgements**

466 Dan Dan Huang acknowledges the financial support from the National Key Research and Development Program of China
467 (2022YFC3703600), the Science and Technology Commission of Shanghai Municipality (21230711000) and the General
468 Fund of Natural Science Foundation of China (42275124). Yong Jie Li acknowledges the financial support from Science and
469 Technology Development Fund, Macau SAR (File No. 0031/2023/AFJ and 0107/2023/RIA2) and multiyear research grants
470 (No. MYRG-GRG2023-00008-FST-UMDF and MYRG-GRG2024-00032-FST-UMDF) from the University of Macau.

471 **References**

472 Atkinson, R. and Arey, J.: Atmospheric degradation of volatile organic compounds, Chem. Rev., 103, 4605-4638, doi:
473 10.1021/cr0206420, 2003.

474 Atkinson, R., Baulch, D. L., Cox, R. A., Crowley, J. N., Hampson, R. F., Hynes, R. G., Jenkin, M. E., Rossi, M. J., and Troe,
 475 J.: Evaluated kinetic and photochemical data for atmospheric chemistry: Volume II—gas phase reactions of organic species,
 476 *Atmos. Chem. Phys.*, 6, 3625-4055, doi: 10.5194/acp-6-3625-2006, 2006.

477 Barmet, P., Dommen, J., DeCarlo, P., Tritscher, T., Praplan, A., Platt, S., Prévôt, A., Donahue, N., and Baltensperger, U.: OH
 478 clock determination by proton transfer reaction mass spectrometry at an environmental chamber, *Atmospheric Measurement*
 479 *Techniques*, 5, 647-656, 2012.

480 Burkholder, J. B., Sander, S. P., Abbatt, J. P. D., Barker, J. R., Cappa, C., Crounse, J. D., Dibble, T. S., Huie, R. E., Kolb, C.
 481 E., Kurylo, M. J., Orkin, V. L., Percival, C. J., Wilmouth, D. M., and Wine, P. H.: Chemical kinetics and photochemical data
 482 for use in atmospheric studies, Evaluation Number 19, Pasadena, CA: Jet Propulsion Laboratory, National Aeronautics and
 483 Space Administration, <http://jpldataeval.jpl.nasa.gov>, 2020.

484 Cao, J., Wang, Q., Li, L., Zhang, Y., Tian, J., Chen, L. A., Ho, S. S. H., Wang, X., Chow, J. C., and Watson, J. G.: Evaluation
 485 of the oxidation flow reactor for particulate matter emission limit certification, *Atmos. Environ.*, 224, 117086, doi:
 486 10.1016/j.atmosenv.2019.117086, 2020.

487 Cheng, X., Chen, Q., Jie Li, Y., Zheng, Y., Liao, K., and Huang, G.: Highly oxygenated organic molecules produced by the
 488 oxidation of benzene and toluene in a wide range of OH exposure and NO_x conditions, *Atmos. Chem. Phys.*, 21, 12005-12019,
 489 doi: 10.5194/acp-21-12005-2021, 2021.

490 Cheng, X., Li, Y. J., Zheng, Y., Liao, K., Koenig, T. K., Ge, Y., Zhu, T., Ye, C., Qiu, X., and Chen, Q.: Oxygenated organic
 491 molecules produced by low-NO_x photooxidation of aromatic compounds: contributions to secondary organic aerosol and steric
 492 hindrance, *Atmos. Chem. Phys.*, 24, 2099-2112, doi: 10.5194/acp-24-2099-2024, 2024.

493 Clerc, M. and Barat, F.: Kinetics of CO formation studied by far-UV flash photolysis of CO₂, *J. Chem. Phys.*, 46, 107-110,
 494 doi: 10.1063/1.1840358, 1967.

495 Cocker, D. R., Flagan, R. C., and Seinfeld, J. H.: State-of-the-art chamber facility for studying atmospheric aerosol chemistry,
 496 *Environ. Sci. Technol.*, 35, 2594-2601, doi: 10.1021/es0019169, 2001.

497 Cohen, N. and Heicklen, J.: The Oxidation of Inorganic Non-metallic Compounds, in: *Reactions of Non-Metallic Inorganic*
 498 *Compounds*, *Compr. Chem. Kinet.*, 1-137, doi: 10.1016/s0069-8040(08)70303-0, 1972.

499 Ehhalt, D. H.: Photooxidation of trace gases in the troposphere Plenary Lecture, *Phys. Chem. Chem. Phys.*, 1, 5401-5408, doi:
 500 10.1039/A905097C, 1999.

501 Friedman, B. and Farmer, D. K.: SOA and gas phase organic acid yields from the sequential photooxidation of seven
 502 monoterpenes, *Atmos. Environ.*, 187, 335-345, doi: 10.1016/j.atmosenv.2018.06.003, 2018.

503 Fuchs, H., Tan, Z., Lu, K., Bohn, B., Broch, S., Brown, S. S., Dong, H., Gomm, S., Häsel, R., and He, L.: OH reactivity at a
 504 rural site (Wangdu) in the North China Plain: contributions from OH reactants and experimental OH budget, *Atmos. Chem.*
 505 *Phys.*, 17, 645-661, doi: 10.5194/acp-17-645-2017, 2017.

506 George, I. J., Vlasenko, A., Slowik, J. G., Broekhuizen, K., and Abbatt, J. P. D.: Heterogeneous oxidation of saturated organic
 507 aerosols by hydroxyl radicals: uptake kinetics, condensed-phase products, and particle size change, *Atmos. Chem. Phys.*, 7,
 508 4187-4201, doi: 10.5194/acp-7-4187-2007, 2007.

509 Hildebrandt, L., Donahue, N. M., and Pandis, S. N.: High formation of secondary organic aerosol from the photo-oxidation of
 510 toluene, *Atmos. Chem. Phys.*, 9, 2973-2986, doi: 10.5194/acp-9-2973-2009, 2009.

511 Kang, E., Root, M. J., Toohey, D. W., and Brune, W. H.: Introducing the concept of potential aerosol mass (PAM), *Atmos.*
 512 *Chem. Phys.*, 7, 5727-5744, doi: 10.5194/acp-7-5727-2007, 2007.

513 Lambe, A. T., Ahern, A. T., Williams, L. R., Slowik, J. G., Wong, J. P. S., Abbatt, J. P. D., Brune, W. H., Ng, N. L., Wright,
 514 J. P., and Croasdale, D. R.: Characterization of aerosol photooxidation flow reactors: heterogeneous oxidation, secondary
 515 organic aerosol formation and cloud condensation nuclei activity measurements, *Atmos. Meas. Tech.*, 4, 445-461, doi:
 516 10.5194/amt-4-445-2011, 2011.

517 Li, R., Palm, B. B., Ortega, A. M., Hlywiak, J., Hu, W., Peng, Z., Day, D. A., Knote, C., Brune, W. H., and De Gouw, J. A.:
 518 Modeling the radical chemistry in an oxidation flow reactor: Radical formation and recycling, sensitivities, and the OH
 519 exposure estimation equation, *J. Phys. Chem. A*, 119, 4418-4432, doi: 10.1021/jp509534k, 2015.

520 Liao, K., Chen, Q., Liu, Y., Li, Y. J., Lambe, A. T., Zhu, T., Huang, R.-J., Zheng, Y., Cheng, X., and Miao, R.: Secondary
 521 organic aerosol formation of fleet vehicle emissions in China: Potential seasonality of spatial distributions, *Environ. Sci.*
 522 *Technol.*, 55, 7276-7286, doi: 10.1021/acs.est.0c08591, 2021.

523 Liu, J., Chu, B., Chen, T., Liu, C., Wang, L., Bao, X., and He, H.: Secondary organic aerosol formation from ambient air at an
 524 urban site in Beijing: effects of OH exposure and precursor concentrations, *Environ. Sci. Technol.*, 52, 6834-6841, doi:
 525 10.1021/acs.est.7b05701, 2018.

526 Liu, T., Clegg, S. L., and Abbatt, J. P.: Fast oxidation of sulfur dioxide by hydrogen peroxide in deliquesced aerosol particles,
 527 *Proceedings of the National Academy of Sciences*, 117, 1354-1359, 2020.

528 Lou, S., Holland, F., Rohrer, F., Lu, K., Bohn, B., Brauers, T., Chang, C. C., Fuchs, H., Häseler, R., and Kita, K.: Atmospheric
 529 OH reactivities in the Pearl River Delta–China in summer 2006: measurement and model results, *Atmos. Chem. Phys.*, 10,
 530 11243-11260, doi: 10.5194/acp-10-11243-2010, 2010.

531 Lu, K., Zhang, Y., Su, H., Brauers, T., Chou, C. C., Hofzumahaus, A., Liu, S. C., Kita, K., Kondo, Y., and Shao, M.: Oxidant
 532 (O₃ + NO₂) production processes and formation regimes in Beijing, *J. Geophys. Res.: Atmospheres*, 115, doi:
 533 10.1029/2009JD012714, 2010.

534 Mao, J., Ren, X., Brune, W. H., Olson, J. R., Crawford, J. H., Fried, A., Huey, L. G., Cohen, R. C., Heikes, B., and Singh, H.
 535 B.: Airborne measurement of OH reactivity during INTEX-B, *Atmos. Chem. Phys.*, 9, 163-173, doi: org/10.5194/acp-9-163-
 536 2009, 2009.

537 Nakashima, Y., Kamei, N., Kobayashi, S., and Kajii, Y.: Total OH reactivity and VOC analyses for gasoline vehicular exhaust
 538 with a chassis dynamometer, *Atmos. Environ.*, 44, 468-475, doi: 10.1016/j.atmosenv.2009.11.006, 2010.

539 Ono, R., Nakagawa, Y., Tokumitsu, Y., Matsumoto, H., and Oda, T.: Effect of humidity on the production of ozone and other
 540 radicals by low-pressure mercury lamps, *J Photochem Photobiol, A*, 274, 13-19, doi: 10.1016/j.jphotochem.2013.09.012, 2014.

541 Palm, B. B., de Sá, S. S., Day, D. A., Campuzano-Jost, P., Hu, W., Seco, R., Sjostedt, S. J., Park, J.-H., Guenther, A. B., and
 542 Kim, S.: Secondary organic aerosol formation from ambient air in an oxidation flow reactor in central Amazonia, *Atmospheric*
 543 *Chemistry and Physics*, 18, 467-493, 2018.

544 Peng, Z. and Jimenez, J. L.: KinSim: a research-grade, user-friendly, visual kinetics simulator for chemical-kinetics and
 545 environmental-chemistry teaching, *J. Chem. Educ.*, 96, 806– 811, doi: 10.1021/acs.jchemed.9b00033, 2019.

546 Peng, Z. and Jimenez, J. L.: Radical chemistry in oxidation flow reactors for atmospheric chemistry research, *Chem. Soc. Rev.*,
 547 49, 2570-2616, doi: 10.1039/C9CS00766K, 2020.

548 Peng, Z., Day, D. A., Stark, H., Li, R., Lee-Taylor, J., Palm, B. B., Brune, W. H., and Jimenez, J. L.: HO_x radical chemistry
 549 in oxidation flow reactors with low-pressure mercury lamps systematically examined by modeling, *Atmos. Meas. Tech.*, 8,
 550 4863-4890, doi: 10.5194/amt-8-4863-2015, 2015.

551 Peng, Z., Day, D. A., Ortega, A. M., Palm, B. B., Hu, W., Stark, H., Li, R., Tsigaridis, K., Brune, W. H., and Jimenez, J. L.:
 552 Non-OH chemistry in oxidation flow reactors for the study of atmospheric chemistry systematically examined by modeling,
 553 *Atmos. Chem. Phys.*, 16, 4283-4305, doi: 10.5194/acp-16-4283-2016, 2016.

554 Rowe, J. P., Lambe, A. T., and Brune, W. H.: Effect of varying the $\lambda=185$ and 254 nm photon flux ratio on radical generation
 555 in oxidation flow reactors, *Atmos. Chem. Phys.*, 20, 13417-13424, doi: 10.5194/acp-20-13417-2020, 2020.

556 Seinfeld, J. H. and Pandis, S. N.: Atmospheric chemistry and physics: from air pollution to climate change, John Wiley &
 557 Sons, Inc., ISBN 9781119221166, 2016.

558 Stone, D., Whalley, L. K., and Heard, D. E.: Tropospheric OH and HO₂ radicals: field measurements and model comparisons,
 559 Chem. Soc. Rev., 41, 6348-6404, doi: 10.1039/C2CS35140D, 2012.

560 Tan, Z., Fuchs, H., Lu, K., Hofzumahaus, A., Bohn, B., Broch, S., Dong, H., Gomm, S., Häsel, R., and He, L.: Radical
 561 chemistry at a rural site (Wangdu) in the North China Plain: observation and model calculations of OH, HO₂ and RO₂ radicals,
 562 Atmos. Chem. Phys., 17, 663-690, doi: 10.5194/acp-17-663-2017, 2017.

563 Tan, Z., Rohrer, F., Lu, K., Ma, X., Bohn, B., Broch, S., Dong, H., Fuchs, H., Gkatzelis, G. I., and Hofzumahaus, A.:
 564 Wintertime photochemistry in Beijing: observations of RO_x radical concentrations in the North China Plain during the BEST-
 565 ONE campaign, Atmos. Chem. Phys., 18, 12391-12411, doi: 10.5194/acp-18-12391-2018, 2018.

566 Wang, N., Zannoni, N., Ernle, L., Bekö, G., Wargocki, P., Li, M., Weschler, C. J., and Williams, J.: Total OH reactivity of
 567 emissions from humans: in situ measurement and budget analysis, Environ. Sci. Technol., 55, 149-159, doi:
 568 10.1021/acs.est.0c04206, 2020.

569 Wang, X., Liu, T., Bernard, F., Ding, X., Wen, S., Zhang, Y., Zhang, Z., He, Q., Lü, S., and Chen, J.: Design and
 570 characterization of a smog chamber for studying gas-phase chemical mechanisms and aerosol formation, Atmos. Meas. Tech.,
 571 7, 301-313, doi: 10.5194/amt-7-301-2014, 2014.

572 Yang, Y., Shao, M., Keßel, S., Li, Y., Lu, K., Lu, S., Williams, J., Zhang, Y., Zeng, L., and Nölscher, A. C.: How the OH
 573 reactivity affects the ozone production efficiency: case studies in Beijing and Heshan, China, Atmos. Chem. Phys., 17, 7127-
 574 7142, doi: 10.5194/acp-17-7127-2017, 2017.

575 You, X., Wang, H., Goos, E., Sung, C.-J., and Klippenstein, S. J.: Reaction kinetics of CO + HO₂ → products: ab initio
 576 transition state theory study with master equation modeling, J. Phys. Chem. A, 111, 4031-4042, doi: 10.1021/jp067597a, 2007.

577 Zhang, Z., Xu, W., Lambe, A. T., Hu, W., Liu, T., and Sun, Y.: Insights Into Formation and Aging of Secondary Organic
 578 Aerosol From Oxidation Flow Reactors: A Review, Curr. Pollut. Rep., 1-14, doi: 10.1007/s40726-024-00309-7, 2024.

579